

---

This is an electronic reprint of the original article.  
This reprint may differ from the original in pagination and typographic detail.

Kinyanjui, M. K.; Björkman, T.; Lehnert, T.; Köster, Janis; Krasheninnikov, A.; Kaiser, U.

**Effects of electron beam generated lattice defects on the periodic lattice distortion structure in 1T-Ta S<sub>2</sub> and 1T-TaS e<sub>2</sub> thin layers**

*Published in:*  
Physical Review B

*DOI:*  
[10.1103/PhysRevB.99.024101](https://doi.org/10.1103/PhysRevB.99.024101)

Published: 02/01/2019

*Document Version*  
Publisher's PDF, also known as Version of record

*Please cite the original version:*

Kinyanjui, M. K., Björkman, T., Lehnert, T., Köster, J., Krasheninnikov, A., & Kaiser, U. (2019). Effects of electron beam generated lattice defects on the periodic lattice distortion structure in 1T-Ta S<sub>2</sub> and 1T-TaS e<sub>2</sub> thin layers. *Physical Review B*, 99(2), 1-11. Article 024101. <https://doi.org/10.1103/PhysRevB.99.024101>

---

This material is protected by copyright and other intellectual property rights, and duplication or sale of all or part of any of the repository collections is not permitted, except that material may be duplicated by you for your research use or educational purposes in electronic or print form. You must obtain permission for any other use. Electronic or print copies may not be offered, whether for sale or otherwise to anyone who is not an authorised user.

## Effects of electron beam generated lattice defects on the periodic lattice distortion structure in $1T$ -TaS<sub>2</sub> and $1T$ -TaSe<sub>2</sub> thin layers

M. K. Kinyanjui,<sup>1</sup> T. Björkman,<sup>2</sup> T. Lehnert,<sup>1</sup> J. Köster,<sup>1</sup> A. Krasheninnikov,<sup>3</sup> and U. Kaiser<sup>1</sup>

<sup>1</sup>Central Facility of Electron Microscopy, Ulm University, Ulm, Germany

<sup>2</sup>Department of Natural Sciences, Åbo Akademi, Turku, Finland

<sup>3</sup>Institute of Ion Beam Physics and Materials Research, Helmholtz-Zentrum Dresden-Rossendorf, Dresden, Germany and Department of Applied Physics, Aalto University, 00076 Aalto, Finland



(Received 2 January 2018; revised manuscript received 10 October 2018; published 2 January 2019)

We have investigated the influence of electron beam generated defects on the structure of periodic lattice distortions (PLDs) which accompany charge density wave modulations in  $1T$ -TaS<sub>2</sub> and  $1T$ -TaSe<sub>2</sub>. Lattice defects were generated through irradiation with high-energy electrons in a transmission electron microscope (TEM). Using atomically resolved high-resolution TEM imaging, we investigate the PLD structure and the changes in this structure with prolonged exposure to the electron beam. We observe the formation of dislocationlike topological defects in the PLD structure. Prolonged exposure to the electron beam also leads to an increase in density of these defects. This is also accompanied by an increase in structural disorder of the PLD. Density functional theory calculations were also performed in order to understand sulfur (S) and selenium (Se) vacancy defect formation in  $1T$ -TaSe<sub>2</sub> and  $1T$ -TaS<sub>2</sub> and their effects on the PLD structure. The formation energy of Se/S vacancies was calculated to be lowest for the highly displaced S/Se atoms in the vicinity of PLD maxima. Vacancies formed at the less displaced sites near the PLD minima were found to have lower formation energy. The calculations also showed that an increase in the S/Se vacancies leads to the formation of dislocations and an increase in disorder in the PLD structures. This supports the experimental observations.

DOI: [10.1103/PhysRevB.99.024101](https://doi.org/10.1103/PhysRevB.99.024101)

### I. INTRODUCTION

Charge density waves (CDWs) are periodic modulations of charge density which arise due to instabilities in the Fermi surface of low-dimensional metals [1]. The CDW state is characterized by a charge density wave as well as a periodic lattice distortion (PLD) which is the modulation of atomic positions [1–3]. In both cases, the modulation wave vector is given by  $\mathbf{q} = 2\mathbf{K}_F$ , where  $\mathbf{K}_F$  is the Fermi wave vector. A one-dimensional CDW can therefore be described as [2]

$$\rho(x) = \rho_0 + \rho \cos[\mathbf{q}x + \phi(x)], \quad (1)$$

where  $\rho(x)$  is the modulated charge density,  $\rho_0$  is the background charge density,  $\rho$  is the CDW amplitude,  $\mathbf{q}$  is the wave vector of the CDW, and  $\phi(x)$  is the CDW phase. Quasi-two-dimensional (2D) transition metal dichalcogenides (TMDCs) including  $1T/2H$ -TaSe<sub>2</sub>,  $1T/2H$ -TaS<sub>2</sub>, and  $2H$ -NbSe<sub>2</sub> are low-dimensional metals that exhibit strong CDW distortions whose transition temperature and commensuration varies mainly with temperature, dimension, pressure, or doping [1]. The CDWs can be probed directly using scanning tunnelling microscopy (STM) [4–6]. On the other hand, diffraction and imaging techniques, such as high-resolution and scanning transmission electron microscopy [HR(S)TEM] [7–9], electron [10–13], and neutron and x-ray diffraction [14–16], are only sensitive to the periodic lattice distortions that accompany the CDW.

The CDW condensate has been shown to slide in an electric field, thus contributing to the transport properties of the CDW material [1–3,17,18]. Theory predicts that an incommensu-

rate CDW (ICCDW) should exhibit frictionless sliding in an electric field, leading to Fröhlich-type superconductivity [2,18]. Fröhlich superconductivity is in practice difficult to achieve since the sliding CDW is often pinned by impurities and defects [2,17–19]. It is therefore crucial to investigate the interaction of the CDW with crystalline defects and impurities in order to understand transport properties in CDW materials. The interaction of CDW with crystalline defects and impurities has been investigated indirectly through transport measurements [20] and x-ray diffraction [21–23], as well as directly through real space imaging with STM imaging [24–27]. In most cases these studies have focused on the effects of impurities introduced through cation doping on the CDW state [4,20,24,25,28]. Little attention has been directed towards the effects of chalcogen defects. Here we present a study where *in situ* defect generation capabilities of the TEM have been used to create chalcogen vacancy defects and at the same time determine the effects of these defects on the CDW state through HRTEM imaging. Understanding the effects of the electron beam on the CDW structure is also important since TEM methods are increasingly useful in examining modulated CDW structures at spatial high resolutions [7–9]. Indeed HR(S)TEM methods are some of the few approaches capable of examining the CDW/PLD and atomic structure of freestanding single layers.

Defect creation in the TEM arises from the interactions of the sample with the fast electrons. This may include defect creation through electronic excitations (ionization) or by elastic collisions of the fast electrons with the lattice atoms (knock-on) [29–32]. Other interaction mechanisms include

local heating and charging in insulating compounds [29]. The ionization damage mechanism is dominant at low electron energies [29]. At higher electron energies the generation of vacancies is mostly through the knock-on mechanism. [29] It has been shown that at low electron beam energies below 100 keV, the defects caused by electron beam irradiation in TMDCs include single chalcogen vacancies, divacancies, self-interstitials, and extended defects [30]. Calculations have also shown that the knock-on threshold for heavier atoms such as tantalum (Ta), molybdenum (Mo), and niobium (Nb) atoms is at high electron energies in the order of 500 keV [30]. Therefore, the nature of the atoms and the electron beam energy play a role in determining which atoms are displaced. In the case of  $1T$ -TaS<sub>2</sub>/ $1T$ -TaSe<sub>2</sub> the large mass difference between chalcogen atoms and Ta atoms means S and Se atoms are selectively displaced before the Ta atoms [30,31]. Regardless of the defect creation mechanism, the created defects can migrate, interact, and agglomerate to form extended defects like vacancy lines, grain boundaries at the inversion domains, or holes [32–34]. Mutka *et al.* showed the capability of electron irradiation on the creation of defects in  $1T$ -TaS<sub>2</sub> using extremely high-energy electrons on the order of 2 MeV [35]. However, these very high-energy electrons knock out both the Ta and S atoms from the lattice leading to rapid amorphization of the sample.

Here, we use a much lower accelerating voltage of 80 keV which is much lower than the knock-out threshold of the Ta atom. These imaging conditions are expected to give rise to mainly lattice defects in the form of S/Se single vacancies, divacancies, and extended line defects [30,31]. In addition, we investigate the effects of the created vacancies on the structure of the PLD. The CDW/PLD condensate can be considered to be an independent electronic crystal. This means the CDW/PLD condensate shows a crystallinelike response to crystalline defects through elastic deformation and formation of dislocations, or domain boundaries [2,4,36]. Indeed, atomic resolved electron microscopy has been used to show CDW/PLD dislocations and disorder in charge-ordered transition metal oxides [37]. As we show here, real space imaging of the PLD and analysis with HRTEM provides a method to observe these effects as well the elastic response of the CDW to lattice defects arising from the electron beam in the TEM.

## II. EXPERIMENTAL DETAILS

### A. HRTEM imaging

In this paper we focused on a-few-layers-thick  $1T$ -TaS<sub>2</sub> and  $1T$ -TaSe<sub>2</sub> samples obtained through mechanical exfoliation. The choice of this sample thickness was primarily motivated by the fact that single layers of  $1T$ -TaS<sub>2</sub> and  $1T$ -TaSe<sub>2</sub> materials are readily oxidized which leads to the suppression of the CDW [8]. HRTEM imaging was performed on a FEI Titan 80-300 TEM equipped with an objective lens spherical aberration (Cs) corrector and operated at 80 kV. The field assisted Schottky emitter was operated at a reduced extraction voltage of 2000 V. During HRTEM imaging a small negative aberration coefficient value of  $-20 \mu\text{m}$  and small positive focus were used. To investigate the effects of electron beam

generated defects on the CDW/PLD, successive HRTEM images were obtained at the same sample region at an electron dose on the order of  $\sim 10^6 e^-/\text{nm}^2$ . The exposure time for the acquisition of the HRTEM images was on the order of 1 s. HRTEM image analysis was done using the Gatan DIGITAL MICROGRAPH software as well as the open source software IMAGE J and GWYDDION.

### B. Analyzing the structure of periodic lattice distortion (PLD) from HRTEM images

#### 1. Atomic structure of PLD distorted $1T$ -TaSe<sub>2</sub>/ $1T$ -TaS<sub>2</sub>

Commensurate CDW/PLD modulation is shown by  $1T$ -TaS<sub>2</sub> and  $1T$ -TaSe<sub>2</sub> characterized by a  $\sqrt{13}a_0 \times \sqrt{13}a_0$  superlattice ( $a_0 =$  lattice parameter) at 180 and 300 K, respectively [1]. The atomic structure of the commensurate CDW (CCDW) distorted  $1T$ -TaS<sub>2</sub>/ $1T$ -TaSe<sub>2</sub> is described in terms of clusters of displaced Ta atoms known as Star-of-David clusters [14]. In Fig. 1 the solid lines show individual single Star-of-David clusters consisting of 13 Ta atoms. The dotted lines display the  $\sqrt{13}a_0 \times \sqrt{13}a_0$  superlattice which connects four Star-of-David clusters. The depicted PLD modulation results in three inequivalent Ta positions labeled as Ta1, Ta2, and Ta3. Ta1 is at the center of the 13-Ta-atom Star-of-David cluster. There are six Ta2's connected to a Ta1 within the same cluster. The Ta3 is found at the apex of the Star-of-David cluster [14].

Maximum Ta distortion/displacement is found at position Ta3. The Ta1 atom found at the center of the cluster shows no displacement. PLD distortion also gives rise to the displacement of Se atoms in a manner similar to Ta atom displacement. This results in five Se inequivalent sites. These inequivalent sites are labeled as Se1–Se5 in Fig. 1. The maximum displacement/distortion of S/Se atoms is in the vicinity of the Ta3 which is found at the apex of the Star-of-David (PLD maxima) [14].

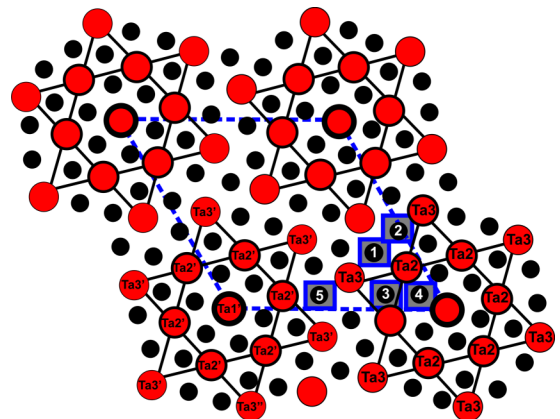


FIG. 1. A schematic showing the atomic structure of the PLD distorted  $1T$ -TaSe<sub>2</sub>. The solid lines show single Star-of-David clusters consisting of 13 Ta atoms each. The dotted line shows the  $\sqrt{13}a_0 \times \sqrt{13}a_0$  superlattice which connects four Star-of-David clusters. Ta atoms are depicted using large solid circles while Se atoms are depicted using small solid circles and squares. The inequivalent Ta sites are labeled, Ta1, Ta2, and Ta3. The inequivalent Se sites are marked with a square and labeled 1–5 for Se positions Se1–Se5, respectively.

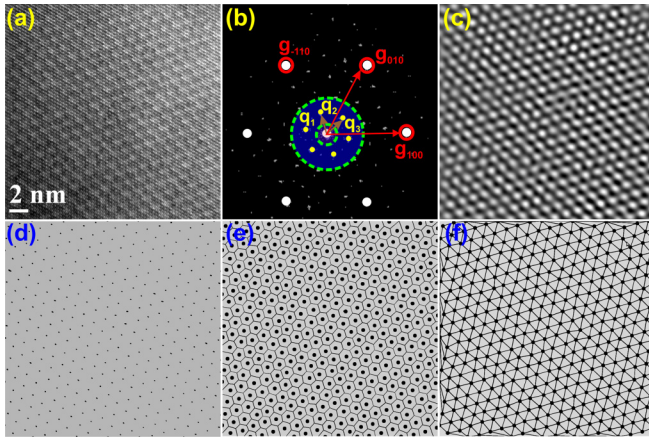


FIG. 2. (a) HRTEM image of  $1T$ -TaSe<sub>2</sub> showing intensity modulation due to the PLD. (b) Fourier transform (FT) pattern of the HRTEM image with the reflections from the underlying  $1T$ -TaSe<sub>2</sub> structure ( $g_{010}$ ,  $g_{100}$ ,  $g_{-110}$ ) and  $q_1$ ,  $q_2$ ,  $q_3$  superlattice spots (within the dashed circle). In the FT pattern  $|q_i| \sim 0.81 \text{ \AA}^{-1}$  a Gaussian mask (dashed circles) selecting the superlattice spots is also shown. (c) PLD structure obtained selecting the superlattice reflections  $q_1$ ,  $q_2$ ,  $q_3$  with the circular Gaussian mask followed by inverse FT. (d) PLD maxima; (e) Voronoi and (f) Delaunay diagrams of the PLD maxima.

## 2. HRTEM imaging of the PLD structure

In strongly distorted CDW materials, the effects of atomic displacements associated with the PLD state can be probed in real space using atomically resolved HR(S)TEM imaging or in diffraction (Fourier) space [7,10,37]. Figure 2(a) presents a HRTEM image from PLD distorted  $1T$ -TaSe<sub>2</sub>. The HRTEM image is characterized by a bright, dark contrast modulation of the atomic columns due to the PLD. The corresponding Fourier transform (FT) pattern of the HRTEM image is displayed in Fig. 2(b). The FT pattern is characterized by a central peak;  $g_{100}$ ,  $g_{010}$ ,  $g_{-110}$  spots from the underlying  $1T$ -TaSe<sub>2</sub> structure, and the superlattice spots  $q_1$ ,  $q_2$ ,  $q_3$  due to the PLD modulation. These superlattice reflections arise from three charge density waves with wave vectors  $q_{i=1,2,3}$  where  $|q_{1,2,3}| \approx (1/\sqrt{13})a_0$  [1]. By selecting and masking the superlattice spots  $q_1$ ,  $q_2$ ,  $q_3$  with a circular Gaussian mask [shown by dashed circles in Fig. 2(b)] followed by inverse FT, it is possible to visualize the PLD structure. The inner radius of the circular Gaussian mask used had dimensions of  $\frac{1}{3}|q_i|$  and an outer radius of  $\frac{4}{3}|q_i|$ . Figure 2(c) displays a periodic image showing the PLD structure. In the image the bright and dark regions correspond to the maxima and minima of the PLD, respectively. The distance between respective PLD maxima/minima in the image corresponds to  $\sqrt{13}a_0$ .

## 3. Quantitative HRTEM image analysis of changes in the PLD structure

Theory has shown that a CDW/PLD condensate can be considered to be a deformable 2D electron crystal [2,36]. The strain response of the CDW/PLD condensate is therefore analogous to be elastic deformation observed in real crystals. It has been shown that the elastic response of the CDW is as a result of interactions of the CDW with crystalline defects [4].

Prolonged exposure of  $1T$ -TaSe<sub>2</sub>/ $1T$ -TaS<sub>2</sub> layers to the electron beam leads to the formation of S/Se single vacancies, divacancies, and extended defects. We therefore expect the CDW/PLD to show an elastic response to these electron beam induced defects [30,31,35]. Isolating the PLD therefore enables the analysis of the structural deformation in the PLD that may arise due to interactions with defects induced by the electron beam. Here we use geometrical phase analysis (GPA) of PLD distorted HRTEM images as well as Voronoi/Delaunay analysis of the PLD structure to study these deformations of the PLD structure. GPA is a quantitative image analysis method which has been successfully used to analyze strain and deformations in atomic scale HR(S)TEM images [38,39]. GPA analysis gives a 2D strain tensor  $\varepsilon_{ij}$  with components  $\varepsilon_{xx}$ ,  $\varepsilon_{yy}$  and shear strain component  $\varepsilon_{xy}$  as well as the rotation  $\omega_{xy}$ . In particular, GPA also provides information regarding structural deformations around topological defects such as domains, grain boundaries, and dislocations [38]. It can therefore be used to identify these topological defects in atomic scale images. GPA has also been extended to study changes in modulated superstructures arising from charge ordering and octahedral tilts in transition metal oxides [40,41]. In this paper GPA analysis of the PLD structure is done following the procedure used for HR(S)TEM images [38]. This involves the calculation of the squared modulus of FT from the HRTEM of the PLD modulated  $1T$ -TaSe<sub>2</sub> and  $1T$ -TaS<sub>2</sub> structure. As shown in Fig. 2(b), the resulting pattern consists of superlattice spots from the PLD and the underlying  $1T$ -TaSe<sub>2</sub> structure. The superlattice and main spots represent the periodicities in the main structure and the PLD structure, respectively. Furthermore, the structure and the shape of the spots are related to the distortions present in the respective lattices. Gaussian masks are then used to select a pair of noncollinear superlattice spots and subsequently the strain maps are calculated as described in the literature [38]. The size of the mask used was  $0.5 \text{ nm}^{-1}$ . This then corresponds to a real space spatial resolution of 2 nm. The effects of the mask size in the GPA calculations are presented in the Supplemental Material [42]. In this paper a Digital Micrograph script was used for GPA strain analysis [43].

Complementary to GPA analysis, topological defects in the PLD are also visualized and analyzed using Voronoi and Delaunay triangulation of the PLD structure [4]. The Voronoi diagram of the PLD structure is created by defining the location of the maxima/minima in the PLD image. The maxima of the PLD are shown in Fig. 2(d). Connecting each PLD maximum with all of the nearest neighbors results in a Delaunay diagram. Perpendicular bisection of the lines joining each PLD maxima/minima to the nearest PLD maxima/minima gives the Voronoi diagram of the PLD structure. An undamaged PLD structure can be considered to be a triangular lattice where each maxima/minima point has six nearest neighbors. The Voronoi diagram of an undamaged PLD lattice therefore consists of hexagons [4]. On the other hand a defected lattice results in the number of nearest neighbors being larger or smaller than six. This results in polygons which are greater or smaller than a hexagon. Similarly, the Delaunay diagram of a defect-free PLD structure consists of PLD maxima with a coordination of six nearest maxima. This coordination is then larger or smaller than 6

in defected PLD structures. Voronoi and Delaunay diagrams of a defect-free PLD structure are shown in Figs. 2(e) and 2(f), respectively. In 2D triangular structures, two types of topological defects can be identified in the Voronoi/Delaunay diagram. This includes disclinations which are represented by single non-six-sided polygons and dislocations which consist of a pair of disclinations [4,44–47]. In this work, the free software IMAGEJ was used to create and analyze Voronoi and Delaunay diagrams from the PLD images.

### C. Density functional calculations

Density functional theory (DFT) calculations were also carried out in order to understand vacancy formation in PLD distorted  $1T$ -TaS<sub>2</sub>/ $1T$ -TaSe<sub>2</sub>. Vacancy formation energies were calculated for different S and Se positions in the CCDW modulated  $1T$ -TaS<sub>2</sub> and  $1T$ -TaSe<sub>2</sub> unit cells. These positions, Se1–Se5, are marked with squares in Fig. 1 [14]. DFT calculations were performed with the projector augmented wave (PAW) method [48] using the Vienna *ab initio* simulation package (VASP) employing the VASP 2012 PAW sets [49,50]. A plane wave basis cutoff of 400 eV was used, and the formation energies were the same within 0.1 eV upon decreasing the cutoff to 300 eV. Defect formation energies of the CDW phase were calculated in  $5 \times 5$  supercells (325 formula units). Models for disordered arrangements of vacancies were constructed using special quasirandom structures [51] in  $4 \times 4$  supercells (208 formula units). For isolated defects and disordered models, only the  $\Gamma$  point was used to sample the Brillouin zone. The atomic positions were relaxed until the maximal residual force was smaller than 5 meV/Å. The vacancy formation energies were calculated with respect to the Se chemical potential of the Se dimer.

## III. RESULTS AND DISCUSSIONS

### A. Experimental results

#### 1. Disorder in the PLD structure

Figure 3(a) displays a HRTEM image from a few layers  $1T$ -TaS<sub>2</sub> obtained at 300 K at an electron dose of  $1.2 \times 10^6 e^-/\text{nm}^2$ . The corresponding FT pattern is displayed in Fig. 3(b). The FT image displays the main reflections from the  $1T$ -TaS<sub>2</sub> structure as well as the superlattice spots arising from the nearly commensurate CDW (NCCDW) modulation characteristic of  $1T$ -TaS<sub>2</sub> at 300 K [1]. Figure 3(c) displays the same sample region after a few seconds of exposure to the electron beam. The corresponding FT pattern after exposure is displayed in Fig. 3(d).

In the FT obtained after prolonged exposure, we observe that the superlattice reflections have become more diffuse but the reflections from the underlying  $1T$ -TaS<sub>2</sub> structure are largely unchanged. At the same time the HRTEM images in Figs. 3(a) and 3(c) show that the layer is still intact. Similarly we explored the evolution of PLD structure in commensurately CDW distorted  $1T$ -TaSe<sub>2</sub>. By using the method to visualize the PLD from the HRTEM images elucidated in the previous section, respective PLDs were also obtained after every exposure. Figures 4(a)–4(c) show successive HRTEM images obtained from the  $1T$ -TaSe<sub>2</sub> layers. The PLDs derived from the respective HRTEM images are shown in Figs. 4(d)–

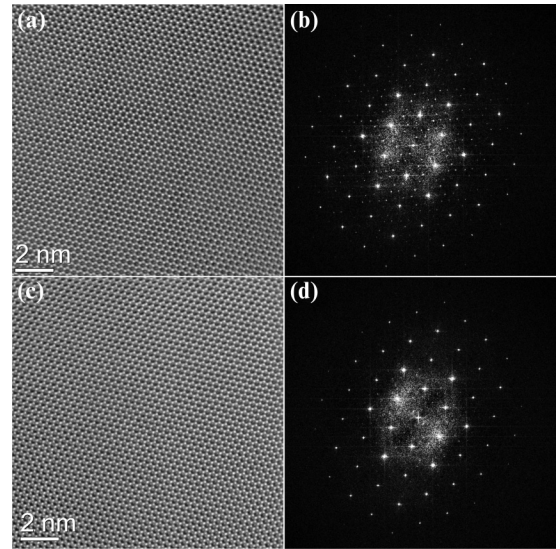


FIG. 3. (a) HRTEM image from a few layers  $1T$ -TaS<sub>2</sub> obtained at 300 K and with an electron dose of  $1.2 \times 10^6 e^-/\text{nm}^2$ . (b) FT image showing the main reflections and the superlattice reflections from the nearly commensurate CDW (NCCDW) modulation. (c) HRTEM image after a few seconds' exposure to the electron beam. (d) FT after exposure to the beam. The superlattice spots have largely disappeared but the spots from the main structure are still visible.

4(f). It can be clearly seen that with increased beam exposure the respective PLD shows increasing disorder.

Increasing structural disorder in the PLD with exposure to the electron beam is also confirmed by autocorrelation (AC)

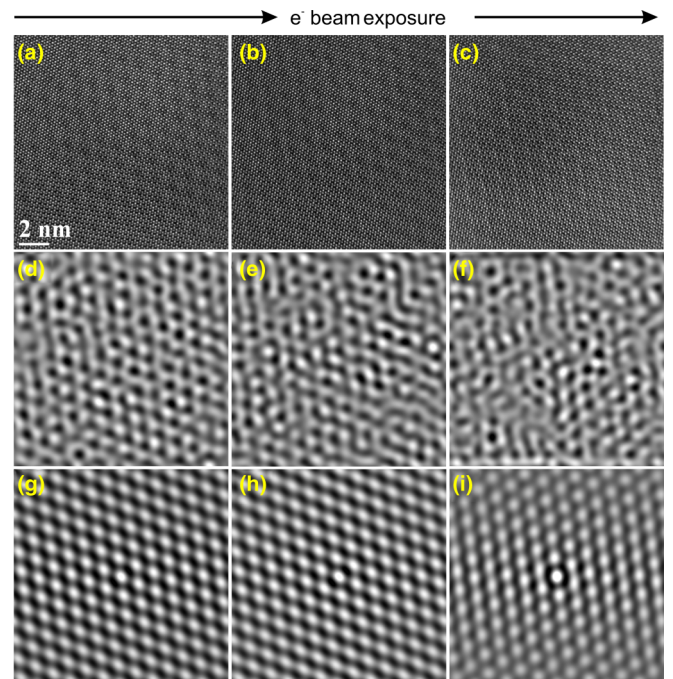


FIG. 4. (a)–(c) Successive HRTEM images obtained at 300 K with an electron dose of  $3.2 \times 10^6 e^-/\text{nm}^2$  from a-few-layer  $1T$ -TaSe<sub>2</sub>. (d)–(f) The corresponding PLD structure obtained from the HRTEM images in (a)–(c), respectively. (g)–(i) Autocorrelation images obtained from the PLD structures in (d)–(f), respectively.

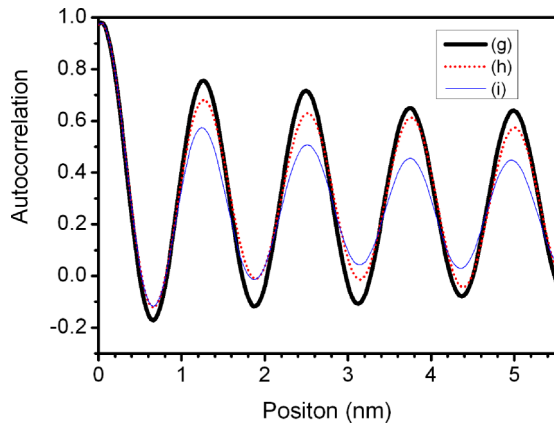


FIG. 5. Intensity profiles obtained from the autocorrelation (AC) images in Figs. 4(g)–4(i). The decrease in the value of AC from (g) to (i) shows increasing disorder in the PLD structure with exposure to the electron beam.

analysis of the PLD images. Autocorrelation analysis has been successfully used on STM images of doped CDW materials to show disorder in the CDW/PLD structure as a function of doping [4,24,25]. Autocorrelation of atomic scale images represents the probability of finding an atom/feature at a position  $r$ , relative to any given atom/feature site in the image [52–54]. This describes how an atomic scale image correlates to itself when the image is displaced with respect to itself in all directions. The value of the AC at a point  $(x, y)$  denotes the autocorrelation with all neighboring points. The center of the AC image is at  $r = 0$  which has an autocorrelation value of 1. In periodic structures characterized by a periodic distance  $r$ , the value of the AC is close to 1 showing a high degree of correlation. On the other hand, the AC value decays rapidly towards zero in disordered structures. The AC images of the respective PLD images are shown in Figs. 4(g)–4(i). In Fig. 5 we show intensity profiles obtained from the AC images presented in Figs. 4(g)–4(i). The AC profiles show periodic patterns reflecting the main periodicity in the PLD. This corresponds to the distance between neighboring PLD maxima/minima, which is also equal to the magnitude of the modulation wave vector. The profiles are also characterized by reduction of AC value with increasing exposure to the electron beam. The decrease in the value of AC from Fig. 4(g) to 4(i) shows increased disorder in the PLD structure with increased beam exposure.

## 2. Defects in the PLD structure

We use Voronoi/Delaunay triangulation and strain mapping with GPA analysis to investigate the presence of topological defects that may occur in the PLD structure as a response to beam exposure. Figures 6(a) and 6(b) show the HRTEM image and FT pattern obtained from the PLD distorted 1T-TaSe<sub>2</sub> layer respectively. The  $g_{100}$ ,  $g_{010}$  spots from the underlying 1T-TaSe<sub>2</sub> structure and the superlattice spots  $q_1$ ,  $q_2$  from the PLD modulation are also marked. We first used the  $g_{100}$  and  $g_{010}$  spots to calculate the  $\epsilon_{xx}$  and  $\epsilon_{yy}$  strain maps for the underlying 1T-TaSe<sub>2</sub> structure. These strain maps are shown in Figs. 6(c) and 6(d), respectively.

Similarly, we also calculated the strain maps for the PLD structure using the superlattice reflections  $q_1$  and  $q_2$ . The  $\epsilon_{xx}$

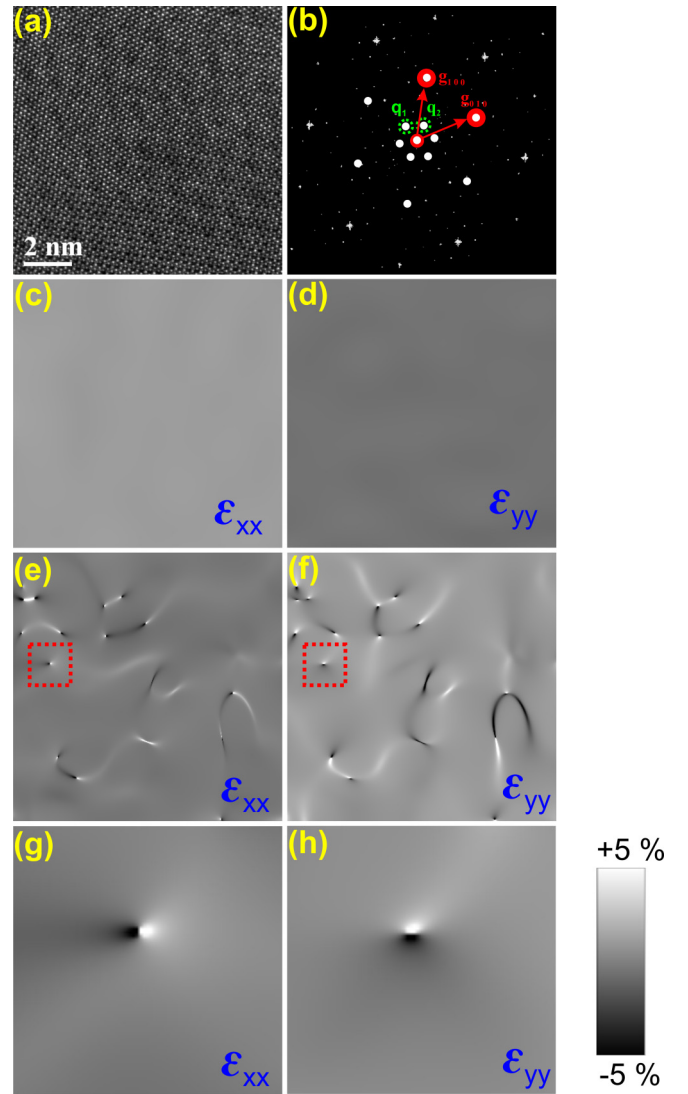


FIG. 6. (a) HRTEM image of 1T-TaSe<sub>2</sub> after exposure to the electron beam obtained at 300 K with an electron dose of  $3.2 \times 10^6 e^-/\text{nm}^2$ . (b) FT pattern obtained from the HRTEM image showing the  $g_{010}$  and  $g_{100}$  reflections from the underlying 1T-TaSe<sub>2</sub> structure. The superlattice spots  $q_1$  and  $q_2$  due to PLD modulation are also marked. (c)  $\epsilon_{xx}$ , (d)  $\epsilon_{yy}$  strain maps calculated from the main 1T-TaSe<sub>2</sub> structure using the  $g_{100}$  and  $g_{010}$  spots. (e)  $\epsilon_{xx}$ , (f)  $\epsilon_{yy}$  strain maps calculated for the PLD structure using the superlattice spots  $q_1$  and  $q_2$ . The dotted square shows a dislocation core in the PLD structure. A dislocation core is shown in more detail in (e),(f) for  $\epsilon_{xx}$  and  $\epsilon_{yy}$ , respectively. The gray scale indicates strain changes of  $-5\%$  to  $+5\%$ .

and  $\epsilon_{yy}$  strain maps derived from the PLD structure are shown in Figs. 6(e) and 6(f), respectively. The dotted square also shows a dislocation core in the PLD structure. A dislocation core in the PLD structure is presented in more details in Figs. 6(e) and 6(f) for  $\epsilon_{xx}$  and  $\epsilon_{yy}$ , respectively. The gray scale indicates strain changes of  $-5\%$  to  $+5\%$  where the positive value is due to tensile strain and the negative value is due to compressive strain. We note that the strain maps for the PLD structure [Figs. 6(e) and 6(f)] are characterized by defects which are not observed in the strain maps obtained from the underlying 1T-TaSe<sub>2</sub> [Figs. 6(c) and 6(d)].

This observation can be explained by the difference in the magnitude of lattice displacements arising from dislocations in the underlying  $1T$ -TaSe<sub>2</sub> structure and in the PLD structure, respectively.

The magnitude and direction of structural distortion arising from a dislocation is represented by the Burgers vector. It has been shown that the magnitude of the Burgers vector for structural dislocations in many two-dimensional TMDCs is on the order of one lattice parameter [47]. On the other hand, as shown in this paper and in the literature, the magnitude of the Burgers vector for a PLD dislocation is on the order of one PLD wavelength [4]. This corresponds to a Burgers vector length of  $\sim 1.25$  nm in  $1T$ -TaSe<sub>2</sub>. As already mentioned the PLD superlattice is several times larger than the unit cell of  $1T$ -TaSe<sub>2</sub>. Therefore the displacement arising from a PLD dislocation in the PLD structure is much larger than the displacement caused by a structural dislocation in the underlying  $1T$ -TaSe<sub>2</sub> structure. In addition to the differences in the magnitude of displacement, the resolution of structural displacement investigated in the GPA method is determined by the radius of the aperture used to select spots in FT. In this work we used masks of radius  $0.5 \text{ nm}^{-1}$  corresponding to a spatial resolution of 2 nm. The GPA spatial resolution used in the calculation is therefore only sufficient to observe displacements in the PLD and not in the underlying  $1T$ -TaSe<sub>2</sub> structure. However, this also enables the PLD structure to be analyzed independently. The minimum radius of the GPA aperture necessary to visualize defects in the strain maps of the underlying  $1T$ -TaSe<sub>2</sub> structure was determined to be  $2 \text{ nm}^{-1}$  [42]. A higher spatial resolution is therefore required to observe defects in the underlying  $1T$ -TaSe<sub>2</sub> structure than in the PLD structure.

In order to confirm the presence of dislocations in the PLD structure we compared the results obtained from GPA to those obtained with Voronoi and Delaunay diagram triangulation. Figures 7(a) and 7(b) display the HRTEM image and the PLD structure derived from  $1T$ -TaSe<sub>2</sub> after exposure to the electron beam. Figure 7(c) shows the Voronoi diagram of the PLD structure. Each point in the Voronoi diagram represents a PLD maxima and the polygon is defined by perpendicular bisectors of the line connecting the maxima to its nearest neighbors. In the defect-free region, the Voronoi diagram consists of hexagons. Defected regions are characterized by non-six-sided polygons which indicate the presence of topological defects in the PLD structure [4]. Two types of topological defects can be identified using this approach, disclinations which are represented by single non-six-sided polygons (4, 5, 7, 8) and dislocations which consist of pairs of 7/5 disclinations. In Fig. 7(c) we have marked single disclinations and disclination pairs using shaded polygons. This is also evident in the corresponding Delaunay diagram shown in Fig. 7(d). In the defect-free region of the PLD structures, the corresponding Delaunay diagram features PLD maxima/minima coordinated to six nearest neighboring maxima/minima. The number of connections to the nearest neighbors is therefore six for defect-free PLD structures. Defects in the PLD then lead to a local maxima coordination of more or less than six. The heptagons, pentagons, and squares shown in the Delaunay diagram represent seven, five, and coordinated sites respectively. Figures 7(e) and 7(f), respectively, display the

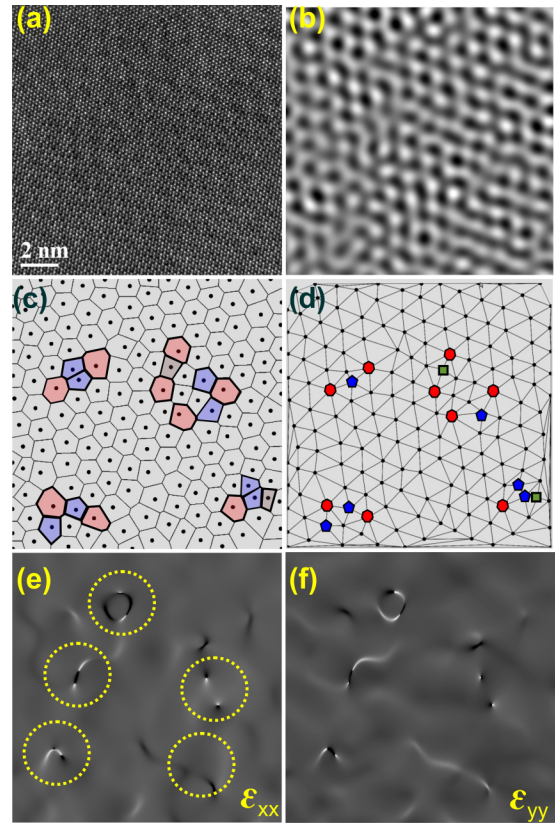


FIG. 7. (a) HRTEM image. (b) PLD structure from  $1T$ -TaSe<sub>2</sub> after electron beam exposure. (c) A Voronoi diagram with PLD maxima as points and polygon defined by perpendicular bisectors of the line connecting the maxima to its nearest neighbors. The shaded polygons represent nonhexagon (4, 5, 7, 8) polygons in the Voronoi diagram. (d) A Delaunay diagram showing the connection between a PLD maximum and the nearest maximum. The heptagons, pentagons, and squares represent seven, five, and four coordinated sites, respectively. Calculated PLD strain showing the presence of dislocations maps for (e)  $\epsilon_{xx}$ , (f)  $\epsilon_{yy}$ . Dislocation cores are marked with dotted circles.

$\epsilon_{xx}$  and  $\epsilon_{yy}$  strain maps calculated for the PLD structure. The regions characterized by PLD dislocation cores are marked with dotted circles.

The Voronoi/Delaunay analysis of a PLD dislocation is shown in more detail in Fig. 8. Figures 8(a)–8(c) respectively

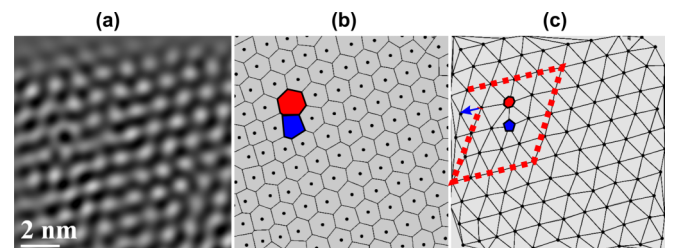


FIG. 8. (a) PLD from  $1T$ -TaSe<sub>2</sub>. (b) Voronoi diagram with dislocations characterized by a 7/5 disclination pair. (c) Delaunay diagram with a possible Burgers circuit around the dislocation. The seven- and fivefold coordinated sites are indicated using a heptagon and pentagon, respectively.

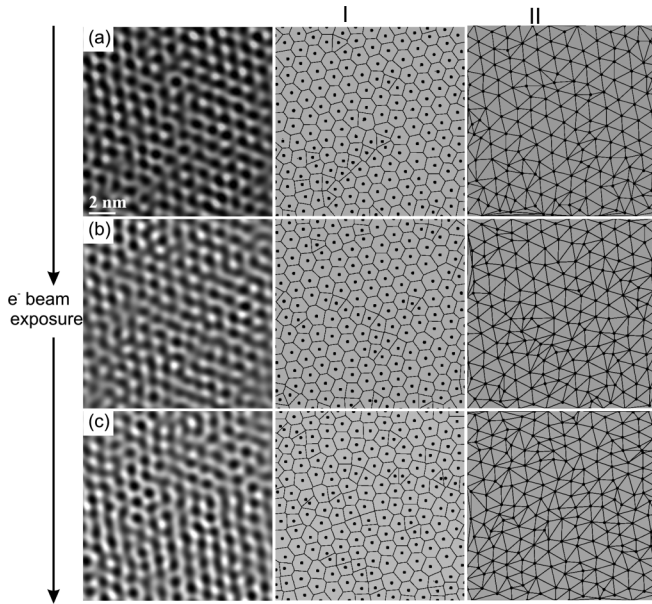


FIG. 9. (a)–(c) Successive PLD structure obtained after increased beam exposure. Panel (I): calculated Voronoi diagram. Panel (II): calculated Delaunay diagram.

display the PLD structure, Voronoi, and Delaunay of a PLD structure with a dislocation. As can be observed in Fig. 8(b), a dislocation is represented by pairs of 7/5 disclinations. The respective Delaunay diagram of the PLD is shown in Fig. 8(c). The Delaunay diagram also displays a Burgers circuit drawn around the PLD dislocation. The magnitude of the Burgers vector is determined from the Delaunay triangulation to be  $\sim 1.23$  nm. This corresponds to one PLD wavelength. Similar results have confirmed that PLD dislocations are characterized by a Burgers vector of magnitude proportional to the wavelength of the PLD modulation [4,37].

Visualization of PLD topological defects through Voronoi/Delaunay analysis presented above also enables the study of their development with increased exposure to the beam. This is shown in more detail in Fig. 9.

Figures 9(a)–9(c) display successive PLD structures [which were also shown in Figs. 5(d)–9(f)] obtained after prolonged beam exposure. Panels (I) and (II) displays the calculated Voronoi and Delaunay diagrams of the PLD structure, respectively. It can be clearly seen that the number of PLD defects including dislocations increases with increased beam exposure. The increase in the density of PLD defects is visible in the increasing number of disclinations that can be observed in the Voronoi (panel I) and Delaunay diagrams (panel II). Comparing the results on PLD defects shown in Fig. 9 with the corresponding autocorrelation plots in Figs. 4(g)–4(i) and 5 we see that a high degree of PLD disorder corresponds to a higher density of PLD defects. We also see that the density of dislocations and PLD disorder increases with exposure to the electron beam.

## B. Comparison with calculations

In the following section we compare the obtained experimental results with the results obtained from DFT calcu-

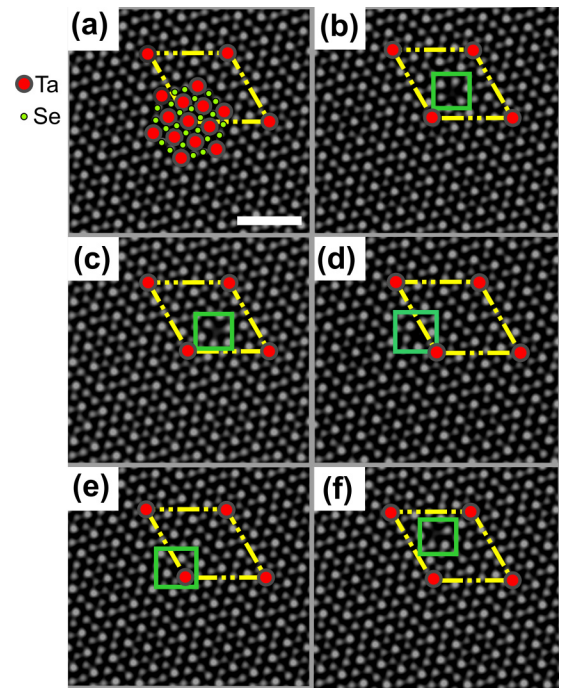


FIG. 10. (a) Calculated HRTEM image from a PLD distorted  $1T$ -TaSe<sub>2</sub> single layer. Image simulation parameters are  $C_s = -15 \mu\text{m}$ , twofold astigmatism  $A_1 = 1$  nm, threefold astigmatism  $A_2 = 50$  nm, coma  $B_2 = 50$  nm, defocus = 8 nm, and focal spread 4 nm. The  $\sqrt{13}a_0 \times \sqrt{13}a_0$  superlattice due to the PLD modulation is shown by the dotted parallelogram. The Star-of-David cluster consisting of 13 Ta atoms (large solid spheres) is also indicated. (b)–(f) Single Se vacancies at the Se atom positions 1–5, respectively. The positions of Se single vacancies in the HRTEM images are marked with squares.

lations. In particular we look at (1) the type and character of defects formed in CDW/PLD distorted  $1T$ -TaSe<sub>2</sub> and  $1T$ -TaS<sub>2</sub> structures, and (2) the effects of these defects on the structure of the periodic lattice distortion.

### 1. Chalcogen vacancy formation in PLD distorted $1T$ -TaS<sub>2</sub>/ $1T$ -TaSe<sub>2</sub> single layers

We calculated the formation energies of chalcogen S and Se single vacancies in PLD distorted  $1T$ -TaSe<sub>2</sub> and  $1T$ -TaS<sub>2</sub> monolayers. The formation energies were calculated for different S and Se positions in PLD modulated single layers. These S/Se positions are labeled as Se1–Se5 and are indicated as squares in Fig. 1 [14]. The positions of the respective single Se vacancies with respect to the distorted atomic structure and PLD are shown in Fig. 10 for a PLD distorted  $1T$ -TaSe<sub>2</sub> single layer. In Fig. 10(a) we display a calculated HRTEM image for modulated  $1T$ -TaSe<sub>2</sub> single layers without any defects. The  $\sqrt{13}a_0 \times \sqrt{13}a_0$  superlattice due to the PLD modulation is indicated by the dotted parallelogram. A Star-of-David cluster consisting of 13 Ta atoms (large solid spheres) and Se atoms (small solid spheres) is also shown. In Figs. 10(b)–10(f) we show calculated HRTEM images for a PLD modulated  $1T$ -TaSe<sub>2</sub> single layer with single Se vacancies at Se positions Se1–Se5, respectively [14].

TABLE I. Formation energies of single S and Se vacancies for different Se shown in Fig. 10. The formation energies for S vacancies in commensurately modulated  $1T$ -TaS<sub>2</sub> are also shown.

S/Se atom position	TaSe <sub>2</sub> , energy (eV)	TaS <sub>2</sub> , energy (eV)
1 Figure 10(b)	1.8	2.3
2 Figure 10(c)	1.9	2.4
3 Figure 10(d)	3.1	3.1
4 Figure 10(e)	2.8	3.0
5 Figure 10(f)	1.5	2.2

The corresponding formation energies of single S and Se vacancies at various inequivalent positions indicated in Fig. 10 are shown in Table I. The formation energies for S vacancies in commensurately modulated  $1T$ -TaS<sub>2</sub> are also included in the table.

As can be deduced in Table I atomic positions Se1, Se2, Se5 have lower vacancy formation energy than positions Se3, Se4. As can be observed in Figs. 1 and 10, positions Se1, Se2, Se5 are at the maxima of the PLD and positions Se3, Se4 are at the minima of the PLD. This is also the case with PLD distorted  $1T$ -TaS<sub>2</sub> structure. In PLD distorted  $1T$ -TaS<sub>2</sub> and  $1T$ -TaSe<sub>2</sub> structures the atoms that have undergone the most displacement are in the vicinity of the Ta3 at the apex of the Star-of-David cluster. Therefore the formation energy of S and Se single vacancies is much lower at these highly distorted sites. On the other hand, atoms at the vicinity of the PLD minima have undergone the least displacement. This corresponds to the atoms in the vicinity of the Ta1 center of a Star-of-David cluster. Consequently, the formation energy of S and Se single vacancies is much higher at these less distorted S and Se sites.

## 2. PLD disorder and defects in calculated structures

In addition, we also calculated the effects of increased Se vacancy defect density on the PLD structure in  $1T$ -TaSe<sub>2</sub> single layers.

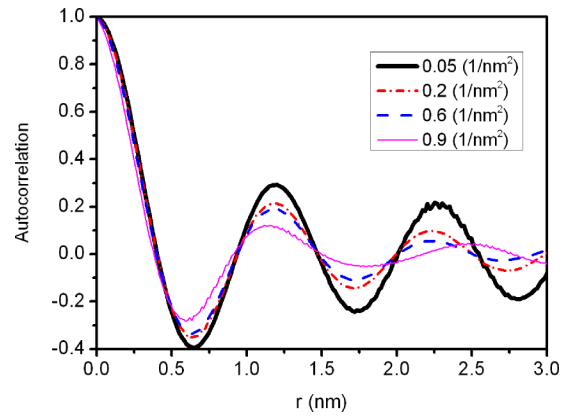


FIG. 12. Decrease in the autocorrelation value of the calculated PLD [Figs. 11(e)–11(h)] with increasing defect density due to increasing disorder.

The upper panel in Fig. 11 displays calculated HRTEM images of single-layer  $1T$ -TaSe<sub>2</sub> layer with increasing Se vacancy defect densities of (a) 0.05 defects ( $1/\text{nm}^2$ ), (b) 0.2 defects ( $1/\text{nm}^2$ ), (c) 0.6 defects ( $1/\text{nm}^2$ ), and (d) 0.9 defects ( $1/\text{nm}^2$ ). The lower panel, (e–h), displays the respective PLD lattices for successively increasing Se defect densities. It can be seen that increasing Se vacancy density leads to the increased disorder in the PLD lattices. This increase in PLD disorder with increase in vacancy defect density is apparent in the autocorrelation plots shown in Fig. 12. The autocorrelation of the calculated PLD lattices shows strong decrease in value with increasing defect densities due to increasing disorder in the PLD.

In Fig. 13 we compare the PLD structure between calculated HRTEM structures for defect-free  $1T$ -TaSe<sub>2</sub> with that of a  $1T$ -TaSe<sub>2</sub> structure characterized by a defect density of  $0.2\ 1/\text{nm}^2$ . The calculated HRTEM image of defect-free PLD distorted  $1T$ -TaSe<sub>2</sub> is shown in Fig. 13(a). The PLD structure and  $\varepsilon_{xx}$ ,  $\varepsilon_{yy}$  strain maps from defect-free  $1T$ -TaSe<sub>2</sub> are shown

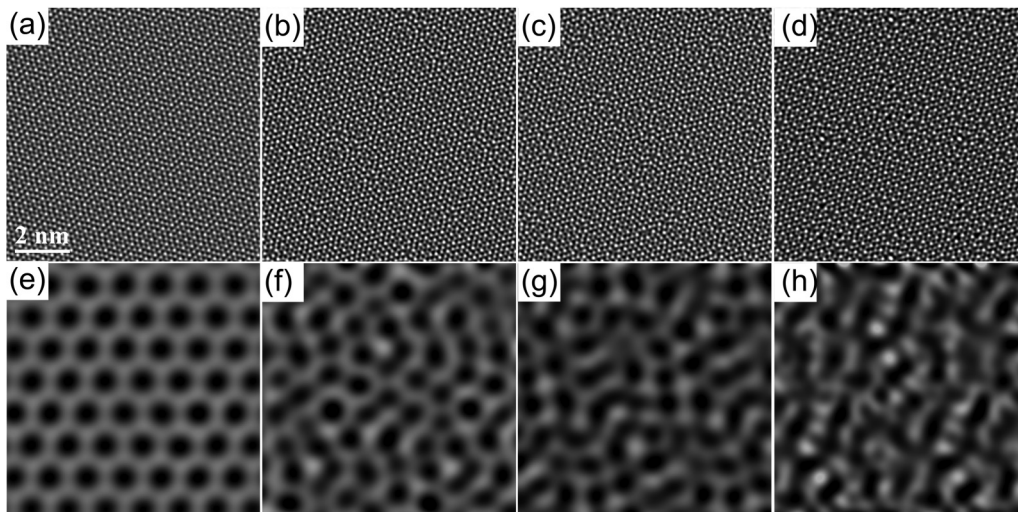


FIG. 11. Calculated HRTEM images for single  $1T$ -TaSe<sub>2</sub> layer for increasing Se vacancy defect densities of (a) 0.05 defects ( $1/\text{nm}^2$ ); (b) 0.2 defects ( $1/\text{nm}^2$ ); (c) 0.6 defects ( $1/\text{nm}^2$ ); (d) 0.9 defects ( $1/\text{nm}^2$ ). (e)–(h) Structure of the PLD for the respective HRTEM image and defect densities.

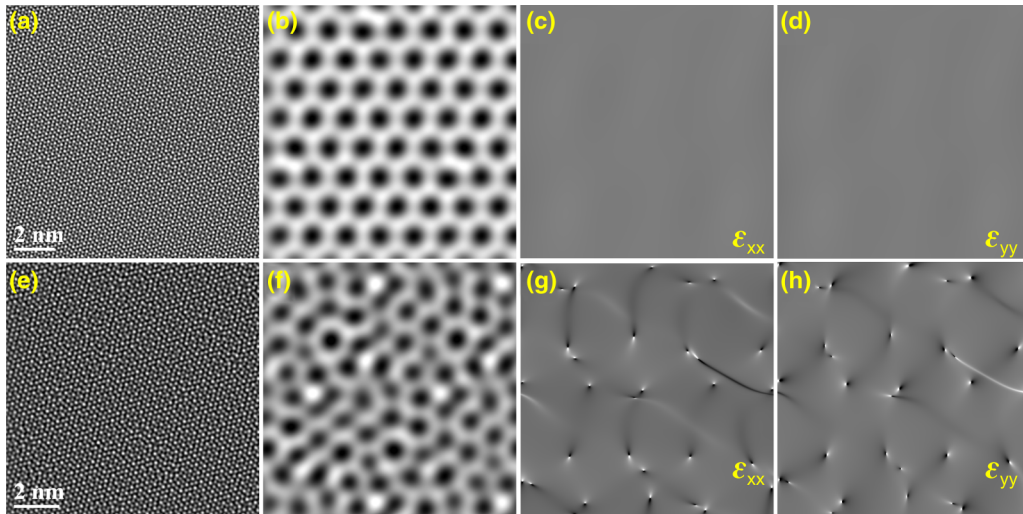


FIG. 13. Calculated (a) HRTEM image, (b) PLD, (c)  $\epsilon_{xx}$ , (d)  $\epsilon_{yy}$ , of a defect-free  $1T$ -TaSe<sub>2</sub>. Calculated (e) HRTEM image (f) PLD, (g)  $\epsilon_{xx}$ , (h)  $\epsilon_{yy}$ , of  $1T$ -TaSe<sub>2</sub> with a defect density of  $0.2 \text{ 1/nm}^2$ .

in Figs. 13(b)–13(d), respectively. The PLD structure of the defect-free  $1T$ -TaSe<sub>2</sub> structure does not show any disorder or defects. Consequently no deformation arising from PLD dislocations can be observed in the respective strain maps. Similarly the calculated HRTEM image of defected PLD distorted  $1T$ -TaSe<sub>2</sub> is shown in Fig. 13(e). The PLD structure,  $\epsilon_{xx}$ , and  $\epsilon_{yy}$  strain maps from defect-free  $1T$ -TaSe<sub>2</sub> are shown in Figs. 13(f)–13(h), respectively. In contrast to the defect-free structure the PLD structure of the defected  $1T$ -TaSe<sub>2</sub> is characterized by disorder and dislocations. This supports the observations made in the experiment.

In the previous section we have used DFT calculations based on single  $1T$ -TaSe<sub>2</sub>/TaS<sub>2</sub> layers in order to understand the effects of S/Se point defects on the CDW structure. On the other hand our experimental results were based on a few layers of both structures. It is clear that the single layer describes the interaction between point defects and CDW quite well. This is the case since in both multilayer and single-layer cases we observed development of dislocations and disorder in the CDW structure with increasing S/Se vacancy defects. In addition, our experiments also agree with previous STM studies which showed CDW dislocations and disorder with increased impurities in the structure [4]. STM is only surface sensitive and therefore does not measure bulk properties. While impurities have been shown to increase disorder in the 3D stacking [55], the main interaction of the CDW with point defects created by the electron beam can be considered to be within the atomic layers. A calculation based on a single layer is therefore a good approximation of the process that happens when a CDW interacts with defects within the atomic layer. Secondly the calculations on the single layers are important in their own since they show a particular trait of point defect formations in CDW distorted structures. They show that defects are preferentially formed at the highly distorted sites.

We have therefore observed two main electron beam induced effects on the PLD structure in  $1T$ -TaSe<sub>2</sub> and  $1T$ -TaS<sub>2</sub>. These include formation of dislocationlike defects and increased structural PLD disorder. It is important to note that

dislocation-type defects and the disorder shown here are in the PLD structure and not the underlying  $1T$ -TaSe<sub>2</sub>/ $1T$ -TaS<sub>2</sub> atomic lattice. In general, the interaction of the CDW with lattice defects has been explained in terms of the interaction between the CDW and possible Friedel oscillations associated with the crystalline defects [21,36,55–62]. Point defects in metals can cause a local Fermi surface instability which results in damped oscillations of the charge density around the defect [56]. These local Friedel oscillations have a period  $\sim 2K_F$  where  $K_F$  is the Fermi wave vector [21,56]. In metallic and CDW distorted dichalcogenides, the point defects and impurities could also result in local Friedel oscillations which also have the same period as the CDW distortion [59]. The interference of the CDW and the Friedel oscillations leads to the phase of the CDW being pinned locally at the crystalline defect. In the present case, the irradiation with an electron beam creates mainly chalcogen localized defects which include vacancies, divacancies, and interstitials as well as extended defects. These defects may pin the phase of the CDW locally inducing strain in the CDW lattice since the CDW reacts elastically by deforming around the defect [61]. With increase in the concentration of defects as a result of prolonged beam exposure, elastic deformation is no longer enough to overcome the pinning energy leading to the formation of topological defects such as dislocations [35]. The number of these CDW defects will increase rapidly with increasing concentration of irradiation defects. With increasing number of defects the CDW becomes more disordered.

#### IV. CONCLUSION

We have investigated the influence of electron beam generated lattice defects on the structure of the periodic lattice distortion (PLD) which accompanies charge density wave modulations in  $1T$ -TaS<sub>2</sub> and  $1T$ -TaSe<sub>2</sub>. We have exploited the *in situ* defect generation capabilities of the electron beam in a transmission electron microscope to create defects, at the same time determining the effects of these defects on the

structure of the PLD. We observe the formation of dislocationlike topological defects in the PLD structure as well as the loss of CDW long-range order with increased exposure to the electron beam. DFT calculations provided insights into the formation of atomic defects in the crystal lattice and also made it possible to assess the effects of increased defect density on the PLD structure. The formation energy of S and Se vacancy defects is found to be lowest in the vicinity of the highly distorted atomic sites and highest at the less distorted atomic site. Increasing the defect density in the DFT calculations is shown to lead to an increase in disorder and defects in the PLD structures, in good agreement with our experimental observations.

## ACKNOWLEDGMENTS

We wish to thank O. Lehtinen for fruitful discussions and valuable suggestions. The authors acknowledge funding from the German Research Foundation (DFG) under Project No. KR 48661 and the Ministry of Science, Research and the Arts (MWK) of the federal state Baden-Württemberg, Germany, in the frame of the SALVE (Sub-Angstroem Low-Voltage) project. A. K also thanks the Academy of Finland for the support under Project No. 286279. We also thank CSC-IT Center for Science Ltd. for generous grants of computer time and PRACE for awarding us access to Hazel Hen at High Performance Computing Center, University of Stuttgart, Germany.

- 
- [1] J. Wilson, F. D. Salvo, and S. Mahajan, *Adv. Phys.* **24**, 117 (1975).
- [2] P. Monceau, *Adv. Phys.* **61**, 325 (2012).
- [3] R. H. Friend and D. Jerome, *J. Phys. C: Solid State Phys.* **12**, 1441 (1979).
- [4] H. Dai and C. Lieber, *Annu. Rev. Phys. Chem.* **44**, 237 (1993); *J. Phys. Chem.* **97**, 2362 (1993).
- [5] B. Giambattista, C. G. Slough, W. W. McNairy, and R. V. Coleman, *Phys. Rev. B* **41**, 10082 (1990).
- [6] A. Manivannan, L. A. Nagahara, M. Tsukada, K. Hashimoto, A. Fujishima, H. Berger, and F. Levy, *Surf. Sci.* **274**, L554 (1992).
- [7] T. Ishiguro and H. Sato, *Phys. Rev. B* **52**, 759 (1995).
- [8] A. W. Tsen, R. Hovden, D. Wang, Y. D. Kim, J. Okamoto, K. A. Spoth, Y. Liu, W. Lu, Y. Sun, J. C. Hone, L. F. Kourkoutis, P. Kim, and A. N. Pasupathy, *Proc. Natl. Acad. Sci. USA* **112**, 15054 (2015).
- [9] D. Sakabe, Z. Liu, K. Suenaga, K. Nakatasugawa, and S. Tanda, *NPJ Quantum Mater.* **2**, 22 (2017).
- [10] J. van Landuyt, G. van Tendeloo, and S. Amelinckx, *Phys. Status Solidi A* **26**, 359 (1974).
- [11] R. L. Withers and J. W. Steeds, *J. Phys. C* **20**, 4019 (1987).
- [12] K. K. Fung, J. W. Steeds, and J. A. Eades, *Physica B (Amsterdam, Neth.)* **99**, 47 (1980).
- [13] C. B. Scruby, P. M. Williams, and G. S. Parry, *Philos. Mag.* **31**, 255 (1975).
- [14] R. Brouwer and F. Jellinek, *Physica B+C (Amsterdam)* **99**, 51 (1980).
- [15] A. Spijkerman, J. L. de Boer, A. Meetsma, G. A. Wiegers, and S. van Smaalen, *Phys. Rev. B* **56**, 13757 (1997).
- [16] D. E. Moncton, J. D. Axe, and F. J. DiSalvo, *Phys. Rev. Lett.* **34**, 734 (1975).
- [17] G. Gruner, *Rev. Mod. Phys.* **60**, 1129 (1988).
- [18] H. Fröhlich, *Proc. R. Soc. A* **223**, 296 (1954).
- [19] H. Fukuyama and P. A. Lee, *Phys. Rev. B* **17**, 535 (1978).
- [20] J. McCarten, D. A. DiCarlo, M. P. Maher, T. L. Adelman, and R. E. Thorne, *Phys. Rev. B* **46**, 4456 (1992).
- [21] S. Rouzière, S. Ravy, J.-P. Pouget, and S. Brazovskii, *Phys. Rev. B* **62**, R16231 (2000).
- [22] D. Le Bolloc'h, V. L. R. Jacques, N. Kirova, J. Dumas, S. Ravy, J. Marcus, and F. Livet, *Phys. Rev. Lett.* **100**, 096403 (2008).
- [23] E. Pinsolle, N. Kirova, V. L. R. Jacques, A. A. Sinchenko, and D. Le Bolloc'h, *Phys. Rev. Lett.* **109**, 256402 (2012).
- [24] S. Brazovskii, C. Brun, Z.-Z. Wang, and P. Monceau, *Phys. Rev. Lett.* **108**, 096801 (2012).
- [25] C. J. Arguello, S. P. Chockalingam, E. P. Rosenthal, L. Zhao, C. Gutiérrez, J. H. Kang, W. C. Chung, R. M. Fernandes, S. Jia, A. J. Millis, R. J. Cava, and A. N. Pasupathy, *Phys. Rev. B* **89**, 235115 (2014).
- [26] A. M. Novello, B. Hildebrand, A. Scarfato, C. Didiot, G. Monney, A. Ubaldini, H. Berger, D. R. Bowler, P. Aebi, and C. Renner, *Phys. Rev. B* **92**, 081101(R) (2015).
- [27] J. I. Okamoto, C. J. Arguello, E. P. Rosenthal, A. N. Pasupathy, and A. J. Millis, *Phys. Rev. Lett.* **114**, 026802 (2015).
- [28] F. J. DiSalvo, J. A. Wilson, B. G. Bagley, and J. V. Waszczak, *Phys. Rev. B* **12**, 2220 (1975).
- [29] R. F. Egerton, P. Li, and M. Malac, *Micron* **35**399 (2004).
- [30] H.-P. Komsa, J. Kotakoski, S. Kurasch, O. Lehtinen, U. Kaiser, and A. V. Krasheninnikov, *Phys. Rev. Lett.* **109**, 035503 (2012).
- [31] Y. Y. Loginov, P. D. Brown, N. Thompson, and K. Durose, *J. Cryst. Growth* **117**, 682 (1992).
- [32] H.-P. Komsa, S. Kurasch, O. Lehtinen, U. Kaiser, and A. V. Krasheninnikov, *Phys. Rev. B* **88**, 035301 (2013).
- [33] O. Lehtinen, H.-P. Komsa, A. Pulkin, M. B. Whitwick, M.-W. Chen, T. Lehnert, M. Mohn, O. V. Yazyev, A. Kis, U. Kaiser, and A. V. Krasheninnikov, *ACS Nano* **9**, 3274 (2015).
- [34] Y.-C. Lin, T. Björkman, H.-P. Komsa, P.-Y. Teng, C.-H. Yeh, F.-S. Huang, K.-H. Lin, J. Jadczyk, Y.-S. Huang, P.-W. Chiu, A. V. Krasheninnikov, and K. Suenaga, *Nat. Commun.* **6**, 6736 (2015).
- [35] H. Mutka, L. Zuppiroli, P. Molinie, and J. C. Bourgoin, *Phys. Rev. B* **23**, 5030 (1981); H. Mutka, *Phase Trans.* **11**, 221 (1988); H. Mutka and P. Molinić, *J. Phys. C* **15**, 6305 (1982); H. Mutka, N. Housseau, L. Zuppiroli, and J. Pelissier, *Philos. Mag. B* **45**, 361 (1982).
- [36] D. Feinberg and J. Friedel, *J. Phys. (Paris)* **49**, 485 (1988).
- [37] B. H. Savitzky, I. El Baggari, A. S. Admasu, J. Kim, S.-W. Cheong, R. Hovden, and L. F. Kourkoutis, *Nat. Commun.* **8**, 1883 (2017).
- [38] M. J. Hÿtch, E. Snoeck, and R. Kilaas, *Ultramicroscopy* **74**, 131 (1998); M. J. Hÿtch, L. Putaux, and J. Thibault, *Philos. Mag.* **86**, 4641 (2006).
- [39] J. Kioseoglou, G. P. Dimitrakopoulou, P. Komninou, T. Karakostas, and E. C. Aifantis, *J. Phys. D: Appl. Phys.* **41**, 035408 (2008).

- [40] J. C. Loudon, L. F. Kourkoutis, J. S. Ahn, C. L. Zhang, S.-W. Cheong, and D. A. Muller, *Phys. Rev. Lett.* **99**, 237205 (2007).
- [41] Y. Zhu, R. L. Withers, L. Bourgeois, C. Dwyer, and J. Etheridge, *Nat. Mater.* **14**, 1142 (2015).
- [42] See Supplemental Material at <http://link.aps.org/supplemental/10.1103/PhysRevB.99.024101> for details on the influence of the mask radius on the GPA analysis.
- [43] C. Koch, GPA script available through <https://www.physics.huberlin.de/en/sem/software>.
- [44] O. V. Yazyev and S. G. Louie, *Phys. Rev. B* **81**, 195420 (2010).
- [45] Y. Liu, X. Zou, and B. I. Yakobson, *ACS Nano* **6**, 7053 (2012).
- [46] F. A. Lavergne, A. Curran, D. G. A. L. Aarts, and R. P. A. Dullens, *Proc. Natl. Acad. Sci. USA* **115**, 6922 (2018).
- [47] X. Zou, Y. Liu, and B. I. Yakobson, *Nano Lett.* **13**, 253 (2013).
- [48] P. E. Blöchl, *Phys. Rev. B* **50**, 17953 (1994).
- [49] G. Kresse and J. Furthmüller, *Comput. Mater. Sci.* **6**, 15 (1996); G. Kresse and D. Joubert, *Phys. Rev. B* **59**, 1758 (1999).
- [50] K. Lejaeghere, G. Bihlmayer, T. Björkman, P. Blaha, S. Blügel, V. Blum, D. Caliste, I. E. Castelli, S. J. Clark, A. D. Corso *et al.*, *Science* **351**, aad3000 (2016).
- [51] A. Zunger, S.-H. Wei, L. G. Ferreira, and J. E. Bernard, *Phys. Rev. Lett.* **65**, 353 (1990).
- [52] G. Y. Fan and J. M. Cowley, *Ultramicroscopy* **17**, 345 (1985).
- [53] R. P. Heilbronner, *Tectonophysics* **212**, 351 (1992).
- [54] D. Necas and P. Klapete, *Ultramicroscopy* **124**, 13 (2013).
- [55] D. E. Moncton, F. J. DiSalvo, J. D. Axe, L. J. Sham, and B. R. Patton, *Phys. Rev. B* **14**, 3432 (1976).
- [56] J. Friedel, *Philos. Mag.* **43**, 153 (1952).
- [57] I. Tüttó and A. Zawadowski, *Phys. Rev. B* **32**, 2449 (1985).
- [58] J. R. Tucker, *Phys. Rev. B* **40**, 5447 (1989).
- [59] J. P. Pouget, *C. R. Phys.* **17**, 332 (2016).
- [60] L. Zuppiroli, H. Mutka, and S. Bouffard, *Mol. Cryst. Liq. Cryst.* **85**, 1 (1982).
- [61] G. Salvetti, C. Roucau, R. Ayroles, H. Mutka, and P. Molinie, *J. Phys. Lett.* **46**, 507 (1985); G. Salvetti, R. Ayroles, H. Mutka, and P. Molinie, in *Charge Density Waves in Solids*, edited by G. Hutiray and J. Solyom, Lecture Notes in Physics Vol. 217 (Springer-Verlag, Berlin, 1985).
- [62] H. Mutka, N. Housseau, J. Pelesier, R. Ayroles, and C. Rancau, *Solid State Commun.* **50**, 161 (1984).